Case Studies in Construction Materials 17 (2022) e01344

Contents lists available at ScienceDirect

Case Studies in Construction Materials

journal homepage: www.elsevier.com/locate/cscm

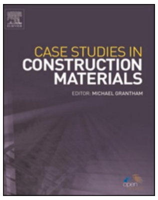

Case study

# De-aluminated metakaolin-cement composite modified with commercial titania as a new green building material for gamma-ray shielding applications

M. Ramadan[a], Mohamed Kohail[b], Aref A. Abadel[c], Yousef R. Alharbi[c], Rabin Tuladhar[d], Alaa Mohsen[e,*]

[a] Chemistry Department, Faculty of Science, Ain Shams University, Cairo, Egypt
[b] Structural Engineering Department, Faculty of Engineering, Ain Shams University, Cairo, Egypt
[c] Department of Civil Engineering, College of Engineering, King Saud University, Saudi Arabia
[d] College of Science & Engineering, James Cook University, QLD 4811, Australia
[e] Faculty of Engineering, Ain Shams University, Cairo, Egypt

ARTICLE INFO

*Keywords:*
Radiation shielding
Titania
Compressive strength
De-aluminated metakaolin

ABSTRACT

Sustainable disposal of dealuminated metakaolin (DAK) is a crucial environmental issue for the alum production industry. In previous studies, DAK was utilized as eco-friendly cementitious materials, but only 10 wt% was used instead of cement as DAK's high percentage has a detrimental effect on the mechanical properties, so the environmental problem of DAK has not yet been solved. In this study, commercial titanium oxide ($TiO_2$) was incorporated in a cement matrix containing DAK that reached 50 wt% to benefit from $TiO_2$'s properties in enhancing the mechanical performance of binding materials and producing cementitious blends used as blocking materials against harmful gamma radiation. Five pastes were prepared to reach the main target; ordinary Portland cement (OPC), OPC-10%DAK (D10), OPC-30%DAK (D30), OPC-50%DAK (D50) and OPC-45%DAK-5%TiO2 (D45-T5). By means of a mini-slump test, all fresh blends have very close flowability using the appreciated additions of polycarboxylate superplasticizer. The hardened composites were cured in tap water for up to 28-days. Compressive strength results at 28 days for OPC, D10, D30 and D50 were 80, 94.6, 60.8 and 57.6 MPa, respectively. An obvious turning point in strength value from 57.6 to 88 MPa after replacement of DAK by 5 wt% $TiO_2$ (D45-T5). A gamma-ray shielding test was performed using two radioactive isotopes (Co-60 and Cs-137). The inclusion of 5% $TiO_2$ has a great impact on the development of shielding power of D45-T5 compared with OPC; the linear attenuation coefficient (μ) values were enhanced from $0.127 \pm 0.003$ $cm^{-1}$ to $0.199 \pm 0.007$ $cm^{-1}$ at 661.6 Kev and from $0.118 \pm 0.003$ $cm^{-1}$ to $0.144 \pm 0.005$ $cm^{-1}$ at 1332.5 Kev. The unique properties of specimens containing the anatase phase may be attributed to the fact that the $TiO_2$ may act as a nano-filler and active seeds for the formation of further hydration products such as CSHs, CAHs and CASHs as detected by X-ray diffraction (XRD), thermal analyses techniques (TGA/DSC) and scanning electron microscope (SEM/EDX). $TiO_2$ caused rearrangement of the textural structure of D45-T5 composite to meso pores, as proved by $N_2$-adsorption/desorption technique. Moreover, the $TiO_2$'s tetragonal structure makes it has dosimetric characteristics of high adsorbent for gamma rays.

---

* Corresponding author.
*E-mail address:* alaa.mohsen@eng.asu.edu.eg (A. Mohsen).

https://doi.org/10.1016/j.cscm.2022.e01344
Received 13 June 2022; Received in revised form 6 July 2022; Accepted 22 July 2022

## 1. Introduction

Radiation technology has become closely linked to progress in industry, agriculture and medicine [1]. The radioactive isotopes used in this technique are known to have unstable and high-energy nuclei that are stabilized by the emission of radiation that interacts with atoms of surrounding materials and cells of living organisms and humans, causing ecosystem disruption [2]. Therefore, protection against these hazardous radiations seems essential. Several factors affect the shielding ability of materials, such as radiation energy, microstructure and density adsorbent materials [3]. Concrete is considered one of the promising materials used in radiation shielding according to its low cost, mass production, easy fabrication and high durability and strength [4].

Portland cement is the primary concrete binding material [5]. The population explosion led to an increase in cement production, which resulted in consuming a high amount of natural resources and energy as well as realizing 5–7% of total $CO_2$ from burning limestone and fossil fuel [6,7]. This coincides with the industrial revolution that polluted the environment through greenhouse gas emissions and the accumulation of huge amounts of waste in landfills, causing water, soil, and air pollution. Significant efforts are being made worldwide to use by-products and waste materials to enhance the implementation of construction materials and reduce costs while also promoting environmental concerns [8,9]. According to ASTMC595/08a [10], most industrial by-products can be categorized as pozzolanic materials such as silica fume (SF) [11], fly ash [12], blast-furnace slag (BFS) [13] and rice husk ash [14], etc. The chemical composition of these by-products, "siliceous or siliceous and aluminous materials," allows them to react with $Ca(OH)_2$ to produce additional hydration products [15]. Generally, the physico-mechanical properties, mix design and curing condition of blended cement produced from the partial replacement of Portland cement with pozzolanic materials are affected by chemical composition, particle size distribution, surface area, morphology and degree of amorphousity of the used industrial by-products.

Kaolin is used in various industries due to its unique physico-chemical properties [16]. Kaolin is an unreactive aluminosilicate precursor; therefore, it is thermally treated between 500 and 800 °C to remove its structural bonded water and form an amorphous structure with a high reactivity [17–19]. Calcination of kaolin leads to the transformation of stable octahedra $AlO_6$ to reactive penta- and tetra coordinated units and then metakaolin (MK) formation [17, 20–22].

Several studies used metakaolin as building materials either in blended cement or geopolymers. Jagtap S. A., et al., 2017 studied the effect of MK on concrete properties. It was found that MK caused decreasing in workability. The optimum percentage of MK to replace cement is 15 wt% as it increased the compressive strength and the flexural strength by 14.3% and 16.5%, respectively, compared with the control specimen after 28 days; beyond 15 wt% MK, the compressive strength decreased [23]. Muduli R. and Mukharjee B. B., 2019 discussed the beneficial effect of partial replacement of MK, which has been linked to its high pozzolanicity and filling effect [24]. Belaid A., et al., 2021 demonstrated that the optimum conditions (calcination temperature and period) for obtaining MK depend on the mineral composition of kaolin. Also, it was evaluated that the 15 wt% MK is enough to replace cement to increase the compressive strength of mortar by 15.6% [25]. Zhang S. et al., 2021 compared the mechanical properties of specimens containing 100 wt% cement, 15 wt% ultra-fine MK and 15 wt% SF instead of cement. It was concluded that there is not much difference in compressive strength between the specimens containing 15 wt% MK and 15 wt% SF [26]. Zidi Z., et al., 2021 assessed the effect of curing conditions on the compressive strength of MK-based geopolymer. It was found that activation of MK required 10 molar sodium hydroxide (NaOH) and sodium silicate ($Na_2SiO_5$ modulus = % $SiO_2/Na_2O$ = 2.5); the ratio of $Na_2SiO_5/NaOH$ = 2 was used to obtain a compressive strength equal 19.9 and 30 MPa at 28 days of curing at 20 and 80 °C, respectively [27]. Ababneh A. et al., 2022 evaluated the effect of kaolin's chemical composition on MK-based geopolymer's compressive strength. The different kaolin samples used contained $SiO_2$ wt% from 41% to 52% and $Al_2O_3$ wt% from 7% to 28%. After calcination at optimum conditions (temperature and pressure) and activation by the alkali-activator, the compressive strength was in the range of 15–40 MPa after 28 days [19].

According to the literature shown above, if MK was used as an alternative to cement or as a basis for geopolymers, then it was not exploited optimally for two main reasons. The first is that many industrial wastes can improve building materials' physico-mechanical and durability properties with the same efficiency as MK and even better, such as SF, FA and GGBFS [15,26,28]. The second is that MK is not waste or by-products; therefore, its engineering values can be well controlled [23], so it must be relied upon in many industries, such as pigment, plastic, ceramics and alum production [16]. It is more likely to benefit from the waste produced from industries based on metakaolin and not the metakaolin itself as building materials, first to benefit from metakaolin in essential industries and secondly to dispose of its waste in a proper manner.

Alum production is one of the leading industries worldwide because of its great importance in many applications such as water treatment [29]. Alum is produced via dealumination of metakaolin by the sulphuric acid leaching process leaving an acidic silicate-rich paste called dealuminated metakaolin (DAK) [30]. A massive amount of DAK is disposed of in the landfill, negatively affecting the surrounding environment [30]. As described above, many studies have been conducted to benefit from MK as a building material. But unfortunately, few of them have been based on waste from industries based on metakaolin. Mostafa et al., 2001 proved that DAK has a superb pozzolanic activity compared with SF, as acid leaching led to an increase in the specific area reaching 90.5 $m^2/g$ and the formation of amorphous active silica [31]. Abo-El-Enein et al., 2013 found that the DAK has a high ability to lime fixation than SF and MK. DAK needed only 12 hrs to fix lime, while MK and SF needed 28 days, which clarifies DAK's high pozzolanicity [17]. Abdelalim et al., 2008 studied the effect of partial replacement of ordinary Portland cement (OPC) with 0, 5, 10, 15 and 20 wt% DAK. It was concluded that DAK led to an increase in the water of consistency reached to 16% increment in specimen containing 20 wt% DAK. For the same specimen (20 wt% DAK), the flowability decreased by 4%. The mechanical properties results evaluated that the optimum replacement percentage of OPC by DAK is 10 wt% [30]. Moselhy, 2018 found that replacement the OPC by 5, 10 and 15 wt% DAK caused a slightly increasing in the compressive strength by 2.7%, 2.1% and 0.6%, respectively [32].

According to the above literature, the first research gap was clarified where only 10 wt% of DAK provided a minor improvement in the mechanical properties which means that the problem of DAK has not been solved as it is still present in large quantities and is not exploited yet. Therefore, it was necessary to search for the addition of other materials to improve the mechanical properties of cement-DAK pastes, especially when replacing cement with large proportions of DAK; also, these materials must have an ability to shield radiation. Titanium oxide ($TiO_2$) is such material that can combine these properties. Some studies showed that the presence of $TiO_2$ in cement matrix composite enhances the hydration characteristics [33,34], mechanical performance [35,36], durability [37,38] and photocatalytic activity [39,40]. Titania has widely participated as a shielding component in different types of glass systems such as $TiO_2$-$CeO_2$–PbO–$B_2O_3$, $Bi_2O_3$–$Na_2O$–$TiO_2$–ZnO–$TeO_2$ and $B_2O_3$ –$SiO_2$ –LiF–ZnO–$TiO_2$. However, its use in the field of construction and concrete as a shielding material was very limited [41–43]. Dezhampanah et al., 2021 and Nikbin et al., 2019 studied the effect of different percentages of $TiO_2$ (0, 2, 4, 6 and 8 wt%) on the compressive strength and radiation shielding ability of heavy-weight concrete (HWC) containing magnetite aggregates. It was evaluated that 6 wt% $TiO_2$ achieved the maximum compressive strength compared with the control specimen (0 wt% $TiO_2$). Liner attenuation coefficient increased with increasing the $TiO_2$ percentage (up to 8 wt%) in the concrete matrix [44,45]. Generally, linear attenuation coefficients (μ) values decreased by temperature up to 600 °C; HWC containing 6% TiO2 NPs possessed the highest gamma shielding capacity compared with the control [46]. It was reported that incorporating $TiO_2$ NPs with the wall of cement pastes up to 50 cm thickness caused notable development in the shielding performance against neutrons of different energy levels (thermal, intermediate and slow) [47].

As illustrated above, the second research gap is that there are very limited studies about the radiation shielding behavior of $TiO_2$ in construction materials. Most of these studies were conducted on HWC-containing aggregate such as magnetite, which already has a significant role in radiation shielding. But there are no or limited studies showing the individual role of $TiO_2$ in the shielding process.

Therefore, the main objective of this work is to study how to benefit advantage of the $TiO_2$ properties in improving the mechanical properties and radiation shielding efficiency of blended cement composites that contain high DAK percentages, which reach 50 wt% as an alternative to cement. This was conducted via measuring the compressive strength, textural characteristics, linear attenuation coefficient, and investigation of hydration products.

## 2. Materials and test methods

### *2.1. Materials*

Ordinary Portland cement (OPC), dealuminated metakaolin (DAK), commercial titanium oxide ($TiO_2$) and poly-carboxylate-based superplasticizer (PCb-SP) were the primary materials used in this work. OPC (42.5 N grade) was obtained from Suez Cement Company, Suez, Egypt. DAK was collected from the Egyptian Shabba Company, Al Qalyubia, Egypt. Commercial $TiO_2$ was supplied by pioneers company for chemicals, Giza, Egypt. PCb-SP "Sika ViscoCrete-3425" was provided by Sika Company, Al Qalyubia, Egypt.

X-ray fluorescence (XRF, model PW-1400, Xios) was used to assess the oxide composition of OPC and DAK; the data are summarized in Table 1. XRF results showed that the main oxide present in OPC were CaO, $SiO_2$ and $Al_2O_{3,}$ with 62.31, 19.20 and 4.90 wt%, respectively. DAK was mainly composed of $SiO_2$ and $Al_2O_3$ with 83.83 and 4.52 wt%, respectively. Therefore, according to the European criteria and specifications, DAK can be considered a pozzolanic material [22,48,49]. X-ray diffraction (XRD, model Xpert-2000, Philips) was used to demonstrate the phase composition for OPC and DAK using a scanning range from $2\theta = 10$–$50°$, with a scanning speed = 1 s/step and resolution = 0.05°/step as in Fig. 1. For OPC, the XRD-pattern composed from sharp peaks indicated to presence of crystalline phases from tricalcium-silicate (alite, $Ca_3SiO_5$, $C_3S$, $2\theta = 25.8$, 30.4, 32.7, 34.9, 38.9 and 41.5°, PDF# 01–070–1846), dicalcium-silicate (belite, $Ca_2SiO_4$, $C_2S$, $2\theta = 29.1$, 32.9, 36.8 and 41.5°, PDF# 01–077–0388), tricalcium-aluminate (aluminate, $Ca_3Al_2O_6$, $C_3A$, $2\theta = 33.3°$, PDF# 00–038–1429) and Tetracalcium-aluminoferrite (celite, $Ca_4Al_2Fe_2O_{10}$, $C_4AF$, $2\theta = 34.1°$, PDF# 01–071–0667). Silicate phases are drastically responsible for cement matrix strength; alite and belite are the active constituents of cement. After hydration, they produced calcium silicate hydrate (C-S-H), which significantly contributes to the hardening of cement [50]. The alite is responsible for early strength (about 7 days of hydration) and the belite is responsible for final strength (about one year) as it is hydrated slower than alite, while the tricalcium-aluminate phase causes the setting [51]. For DAK, the XRD-pattern attains a broad hump between $2\theta = 15$–$26.5°$, which is associated with DAK's amorphous characteristics (highly amorphous silica), indicating its high pozzolanicity. The typical result of an acid assault on MK is the release of free silica and the dissolving of aluminum. As a result, aluminum ions dissolve from the lattice without altering the structure and exposing locations where other metal ions can replace them, which causes an increase in the surface area [52]. The ill-crystalline peaks present are related to kaolinite ($Al_2(OH)_4Si_2O_5$, $2\theta = 12.2$, 19.9, 35.1 and 36.1°, PDF# 00–900–9230), quartz ($SiO_2$, $2\theta = 20.9$, 26, 26.7, 39.3 and 42.2, PDF# 00–005–0490) and anatase ($TiO_2$, $2\theta = 24.9$ and 38.9°, PDF# 01–071–1167). Kaolinite and quartz phases are inactive gradients [53], while the presence of the anatase phase may be a turning point in DAK utilization in construction and building materials applications such as radiation shielding and anti-microbial activity [44,45,54,55]. Fig. 2 demonstrates the particle size distribution for OPC and DAK using a particle size analyzer (PSD: PSS NICOMP Nano analyzer, model N3000); it was noticed that 99% of OPC and DAK particles are less than 14.66 and 11.4 μm in size, respectively. Physico-chemical properties for $TiO_2$ were illustrated using XRD and a scanning electron microscope (SEM/EDX:

**Table 1**
Chemical oxide compositions for OPC and DAK (mass, %).

| Materials | $SiO_2$ | $Al_2O_3$ | $Fe_2O_3$ | CaO | MgO | $TiO_2$ | $SO_3$ | $Na_2O$ | $K_2O$ | $Cl^-$ | LOI |
|---|---|---|---|---|---|---|---|---|---|---|---|
| OPC | 19.20 | 4.90 | 3.60 | 62.31 | 2.41 | 0.00 | 2.82 | 0.41 | 0.63 | 0.09 | 3.63 |
| DAK | 83.83 | 4.52 | 0.50 | 0.15 | 0.09 | 2.98 | 0.85 | 0.03 | 0.05 | 0.06 | 6.94 |

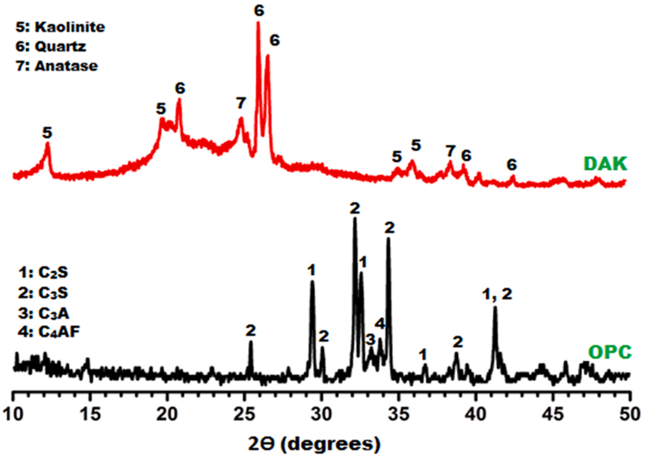

**Fig. 1.** XRD-patterns of OPC and DAK.

ZEISS, model Sigma 300 VP). The XRD-pattern from $2\theta = 10$–$70°$ (Fig. 3) show presence of sharp peaks from the anatase phase ($TiO_2$, $2\theta = 25.9, 37.9, 48, 53.8, 55.1, 62.5$ and $68.4°$ with (101), (112), (200), (105), (211), (204) and (216) diffraction planes, respectively, PDF# 01–071–1167). The average crystallite size for the anatase phase estimated from XRD-pattern is 21 nm, using Debye – Scherrer's equation ($D = 0.9\lambda/\beta\cos\theta$) [56,57]; Where, 0.9: shape factor, $\lambda$: X-ray wavelength, $\beta$: line broadening at half of the maximum intensity in radian (FWHM), and $\theta$: Bragg angle (in degree). The anatase phase a tetragonal structures have a $[TiO6]^{2-}$ octahedra arranged in zigzag chain along (221) diffraction plane, sharing by 4 edges [58].

Also, the SEM/EDX (Fig. 4) represents that the $TiO_2$ particles have a symmetrical shape with a spheroid morphology in the nano range. According to EDX elemental analysis, the commercial titania contains only titanium and oxygen with 43.2% and 56.2% indicating its high purity.

### 2.2. Test methods

Initially, four homogeneous blended cement binders were prepared by mixing OPC with DAK in different percentages in a ball mill for 2 hrs. The four mixes were designed as OPC: DAK in the ratios 100: 0, 90: 10, 70: 30 and 50: 50, coded as OPC (control), D10, D30 and D50, respectively. Another mix was formulated by replacing 5 wt% DAK in the D50 mix with $TiO_2$ (D45-T5), as in Table 2. The OPC paste was prepared using a water/binder (W/B) ratio equal to 0.27 (by mean of Vicat apparatus). While in DAK-containing specimens, the W/B ratio increased to 0.3. Also, variable percentages of PCb-SP were utilized to bring the workability of these

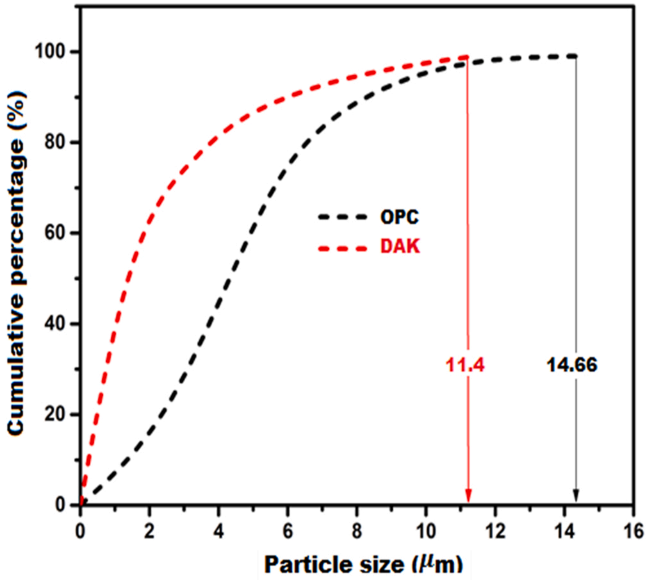

**Fig. 2.** Particle size distribution of OPC and DAK.

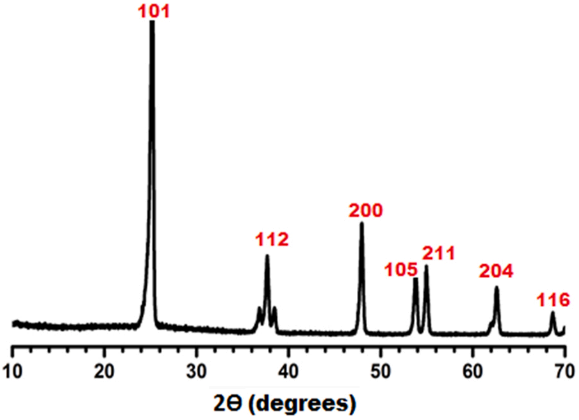

**Fig. 3.** XRD-patterns of $TiO_2$.

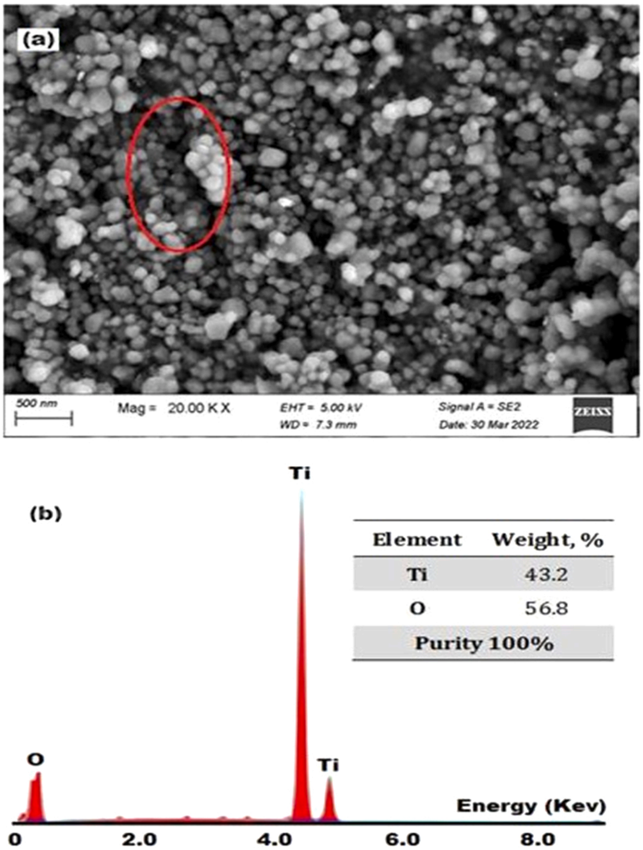

| Element | Weight, % |
|---|---|
| Ti | 43.2 |
| O | 56.8 |
| Purity 100% | |

**Fig. 4.** (a) SEM image and (b) EDX image of $TiO_2$.

**Table 2**
Mix design of the prepared pastes (mass, %).

| Composite | OPC % | DAK% | $TiO_2$% | W/B ratio | SP |
|---|---|---|---|---|---|
| OPC (control) | 100 | – | – | 0.27 | – |
| D10 | 90 | 10 | – | 0.3 | 0.15 |
| D30 | 70 | 30 | – | 0.3 | 0.45 |
| D50 | 50 | 50 | – | 0.3 | 1.00 |
| D45-T5 | 50 | 45 | 5 | 0.3 | 0.80 |

specimens closer to the control paste.

The workability was evaluated via a mini-slump test (ASTMC1161–18) [59]. The paste was cast in Abram's cone with a dimension of 59 ± 1 mm (height), 19 ± 01 mm (top diameter) and 39 ± 1 mm (bottom diameter), then the cone was vertically removed, leaving the paste in the form of a pancake. Finally, the pancake's spread area was measured. For mechanical properties, the control and different blended cement pastes were molded in 25 mm cubic mold and then cured in a humidity chamber (humidity ≈ 98 ± 2%) for 24 hrs. After that, the hardened pastes were demolded and cured under tap water till testing times (3 and 28 days). The compressive strength values were measured using a compression testing machine (maximum load of 60 tons, Controls) according to

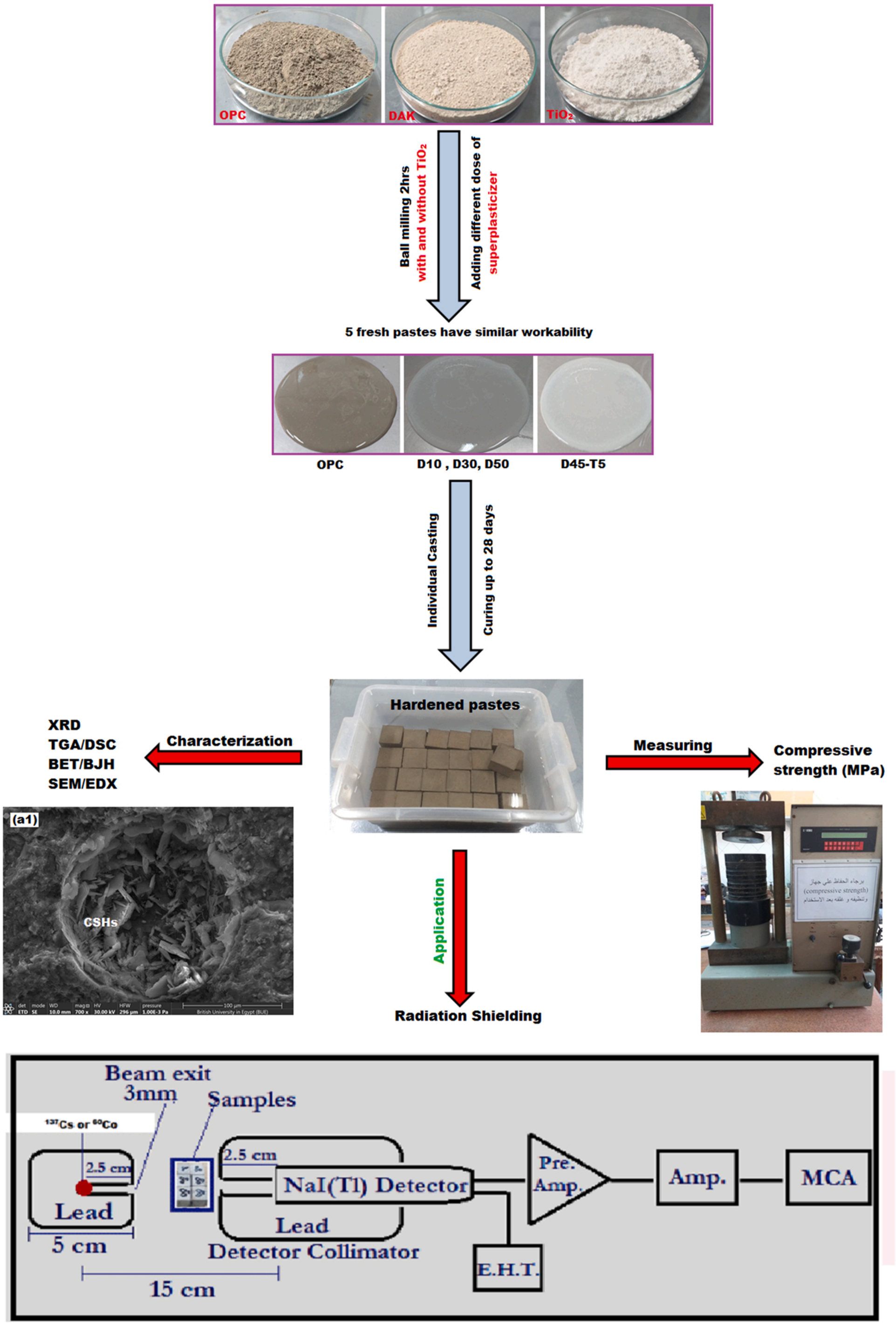

**Fig. 5.** Block diagram for all experimental work.

ASTMC109M-20b [60].

Several instrumental techniques were utilized to investigate the phase composition and morphology of hydration products of hardened specimens, such as XRD, thermo-gravimetric analysis and differential scanning calorimetry (TGA/DSC, Simultaneous Thermogravimetry, model STA 449 F1 Jupiter, NETZSCH) as well as SEM/EDX. $N_2$ gas adsorption-desorption procedure at 77 K measured the textural parameters of hardened pastes using an automatic surface area and pore size distribution analyzer (model BELSORP MINI X, MICROTRAC). The specific surface area ($m^2/g$) was calculated by the Brunauer-Emmett-Teller model (BET). The average pore diameter (nm) and total pore volume ($cm^3/g$) were estimated by the Barrett-Joyner-Halenda model (BJH).

For gamma radiation shielding, linear attenuation coefficients for some selected specimens were measured at two different gamma-ray intensities of 661.64 and 1332.51 Kev emitted from $^{137}Cs$ and $^{60}Co$, respectively. The cubic specimens were located 15 cm far from the isotope source. The influence of specimen thickness on shielding efficiency was measured using different thicknesses (0, 2.5, 5, 7.5, 10, and 12.5 cm) to determine the safe thickness to protect against hazardous gamma radiation. A 3′ × 3′ NaI (TI) detector was used, and then the linear attention coefficient (μ) was calculated using Beer-Lambert's law (Eq. 1).

$$I = I^{\circ} e^{-\mu x} \quad (1)$$

Where; Io and I: incident and transmitted gamma-ray intensities, respectively; μ: linear attention coefficient; and x: thickness of the specimen.

Finally, Fig. 5 displays a block diagram to summarize all of the experimental work.

## 3. Results and discussion

### 3.1. Workability of fresh pastes

The spread area of the fresh pastes in the mini-slump test is usually used as an indicator of their workability; the better workability, the larger spread area is [28,61]. Table 2 and Fig. 6 illustrate the effect of different percentages from DAK and $TiO_2$ on the W/B ratio, PCb-SP wt% and spread area of blended cement paste. It was noticed that the incorporation of DAK in the cement matrix led to increasing the W/B ratio and PCb-SP wt% to attain approximately the same spread area as the control specimen, which is 154, 156, 157, 153 and 156 $cm^2$ for control (OPC), D10, D30, D50 and D45-T5 specimens respectively. Generally, the superplasticizer was adsorbed on the cement particles, enhancing the flowability by preventing flocculating and coalescing between grains. In PCb-SP, adsorption of negative carboxylic groups ($COO^-$) on the cement particle created electrostatic repulsion force between grains, improving workability. The presence of long side chains in PCb-SP would also extend the dispersion of cement particles and hydration products via a steric hindrance effect [62]. It was clarified that increasing DAK wt% in blended cement is accompanied by increasing PCb-SP wt%. This may be attributed to the small particle size, high surface area and the pore characteristics of DAK compared with OPC, which led to entrapped water and decreased workability [30,32]. Therefore, a high percentage of PCb-SP is required to improve workability. In D45-T5, the PCb-SP wt% needed is less than D50 due to the reduction of the DAK wt%. Similar behavior was reported in the investigation of Abdelalim et al., 2008; the replacement of OPC by 20% DAK (whether the treated DAK at pH = 8 or received DAK at pH = 5) caused a notable reduction in the flowability of the fresh mortar due to their higher BET surface areas (40.1 and 42 $m^2/g$, respectively) [30]. Moselhy, 2018 confirmed that the replacement of OPC by 15%DAK affected negatively on the flow behavior of fresh concrete by about 25% reduction (using slump test) due to high porosity of DAK [32]. Ouldkhaoua et al., 2020 concluded that the

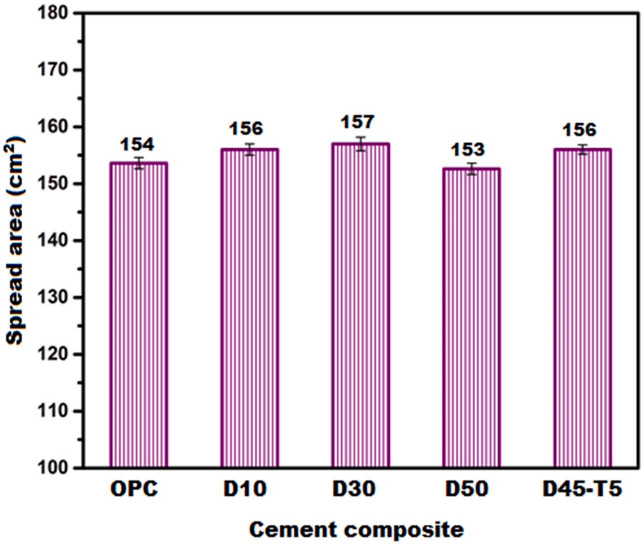

**Fig. 6.** Workability of OPC, OPC-DAK and OPC-45%DAK-5%$TiO_2$ fresh pastes.

replacement of OPC by 15% metakaolin (MK) has required high dose of superplaticizer (1.2%) to give the sample workability of the control fresh mortar. Moreover, the viscosity of the mortar decreased in presence of cathod ray tubes waste glass as fine aggragates; this trend was attributed to high water absorption capacity of MK and low water absorpitivity for most glasses [63].

### 3.2. Mechanical properties of hardened pastes

The compressive strength (CS) for blended cement pasts containing various percentages from DAK (0, 10, 30 and 50 wt%) at different curing times (3 and 28 days) is graphically represented in Fig. 7. It was detected that increasing the curing time led to a significant enhancement in CS results. From 3–28 days, the CS magnitudes were increased by 91.2%, 142.1%, 175.2% and 316.3% for control, D10, D30 and D50, respectively. This may be attributed to a continuous hydration process with curing time that caused the growth of more hydration products such as around the cement grains, filled pores and then gave high CS. The hydration products formed were calcium-silicate-hydrate (C-S-H), calcium-aluminum-hydrate (C-A-H) and calcium-alumino-silicate-hydrate (C-A-S-H) [15,64].

Generally, all blended pastes containing DAK had a lower CS than the control specimen, especially at early hydration age (3 days). This may be correlated to a reduction in OPC content and the pozzolan–$Ca(OH)_2$ reaction has not progressed to the extent required to counteract this effect [65]. Also, it was observed that using 10 wt% DAK in cement matrix enhanced the CS by 16.4% at 28 days. The increment in CS value may be resulted from several factors. DAK's higher pozzolanic activity caused by its lower particle size distribution, higher surface area, and higher pore volume contents resulted in its interaction with $Ca(OH)_2$ produced from the hydration of cement and the formation of further quantity from C-S-H that mainly responsible for the increase in CS [17,31]. Also, the further quantity of DAK may act as an inert filler [66]. The uniform dispersion of DAK resulting from its large dimension sheet prevented its agglomeration and enhanced the mechanical properties [65,67,68]. DAK may behave as a nucleation site to promote the hydration of cementitious materials and then generate more binding phases. Furthermore, the remaining active amorphous silica present in DAK reacts with C-S-H at later ages, produced a low C/S ratio in C-S-H phase which have a high mechanical properties [51,65,69,70]. In contrast, increasing DAK wt% as in D30 and D5 caused a reduction in CS by 23.7% and 26.7%, respectively than the control specimen at 28 days. This may result from excessive OPC dilution by DAK and then generation low binding phase. The same optimized percentage of DAK was reported in the study of Abdelalim et al., 2008 [30] while 15% DAK was reported in the investigation of Moselhy, 2018 [32]. On the contrary, Majstorovic et al., 2022 confirmed that the replacement of OPC by 30%MK enhanced the mechanical characteristics; this high content of MK participated strongly in CH-free cementitious mortar that increased fiber-matrix interface bond [71].

As illustrated above, one of the ways to solve the problem of reduction in CS is using $TiO_2$. Therefore, the effect of DAK replacement in the D50 specimen with 5 wt% $TiO_2$ (D45-T5) on the CS was investigated. It was found that $TiO_2$ enhanced the CS by 49.9% more than the D50 specimen (0 wt% $TiO_2$). Simultaneously, the CS value of the D45-T5 specimen increased by 9.9% than the control specimen despite the noticeable dilution of cement with DAK. This highlights the vital role of $TiO_2$ in enhancing the mechanical performance of cement pastes. As will be proved below by XRD, the $TiO_2$ does not have cementitious characteristics as it is stable and inactive [72]. Thus, the increase in the compressive strength may be resulted from (i) the $TiO_2$ may act as a non-reactive filler due to its lower particle size (≈ 21 nm) that fills the pores and give a compact microstructure [44], (ii) the high surface area of TiO2 make it act as nuclei and seeds available for sedimentation and growth further hydration products [73] and (iii) the $TiO_2$ led to a redistribution of pore structure of the hardened pastes from macro to meso pores. These outcomes are in line with the study of Zhang et al., 2020; 5%

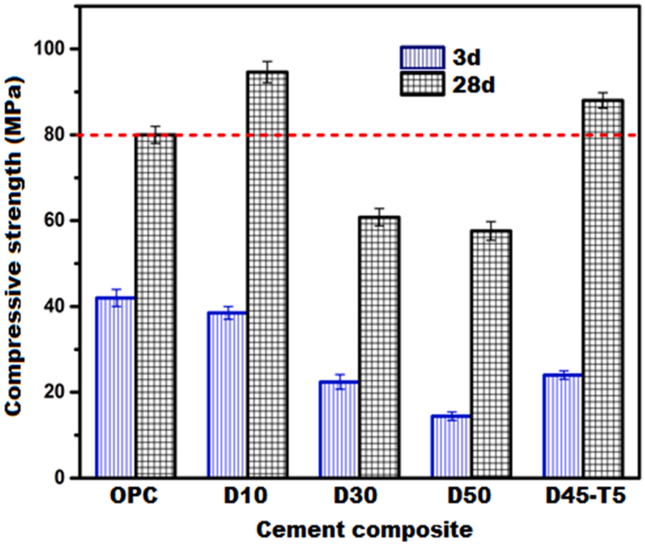

**Fig. 7.** Compressive strength values of OPC, OPC-DAK and OPC-45%DAK-5%$TiO_2$ hardened composites at 3 and 28 days of hydration.

$TiO_2$ NPs accelerated both of hydration reaction and pore-refining, enhanced the compressive strength and mitigated drying shrinkage of cement mortar [74].

## 3.3. Phases identification

### 3.3.1. X-ray diffraction (XRD)

Fig. 8 illustrates XRD-patterns for OPC, OPC-10%DAK (Mix D10), OPC-50%DAK (Mix D50) and OPC-45%DAK-5%$TiO_2$ (Mix D45-T5) composites at 28 days of hydration. XRD-patterns for OPC pastes show different crystalline peaks for the Portlandite phase (CH, $Ca(OH)_2$, PDF# 01–087–0674) that are located at $2\theta = 18.16$, 34.22, 47.20 and 50.89°; this phase is considered one of the main hydration reaction products that are generated during reaction of OPC with water molecules and the existence of it after 28 days represents a good indicator for the growth of hydration reaction [75]. Due to the handling process, small quantities of CH are carbonated and converted into calcite phase (CC, PDF# 01–088–1808) that appears at $2\theta = 29.56$, 41.35 and 47.20 [76]. Calcium silicate hydrate (C-S-Hs, PDF# 00–033–0306) is an essential binding phase that reflects the mechanical behavior; this phase appears at $2\theta = 29.56$ and 30.19°. Unreacted silicate phases such as alite ($C_3S$, PDF# 01–070–1846) and belite ($C_2S$, PDF# 01–077–0388) have crystalline peaks at $2\theta = 28.81$, 32.32, 32.77, 34.51, 39.64 and 41.35°. The same findings and explanations were reported in recent publications [77,78]. Some minor changes have been observed after OPC replacement by 10 wt% DAK (Mix D10). The new crystalline peak appeared at $2\theta = 35.45°$ due to the generation of additional amounts of CSHs. The other crystalline peak appeared at $2\theta = 26.49°$ due to the unreacted quartz phase (PDF# 00–005–0490), representing one of DAK's constituents. The replacement of OPC with 50 wt% DAK led to noticeable changes. Crystalline peaks, distinguished for the Portland phase, have disappeared and at the same time, other new crystalline peaks distinguished for quartz appeared at $2\theta = 20.69$ and 50.13°; this is attributed to the dilution process affecting the OPC hydration negatively [79]. Also, a weak crystalline peak due to the anatase-tetragonal-phase (PDF# 01–071–1167) appeared at $2\theta = 25.25°$. Similar trend was observed in the study of El-Gamal et al., 2017; the replacement of OPC with 20% ceramic waste led to a marked reduction in the content of portlandite [80]. The replacement of 5 wt% DAK by 5 wt% $TiO_2$ (Mix D45-T5) led to the disappearance of unreacted silicates and other additional characteristic peaks for anatase also appeared at $2\theta = 47.85$, 53.79 and 54.95°. The appearance of this phase in abundance was a strong turning point in the mechanical properties of the D45-T5 composite. The studies of Lee and Kurtis, 2010 and Luan et al., 2022 demonstrated that the addition of $TiO_2$ NPs affected positively the early hydration of $C_3S$ and created more nucleation sites [81,82].

### 3.3.2. Thermal analysis (TGA/DSC)

Fig. 9(a-d) displays thermo-gravimetrical analysis (TGA) and differential scanning calorimetry (DSC) for OPC, OPC-10%DAK (Mix D10), OPC-50%DAK (Mix D50) and 50%OPC-45%DAK-5%TiO2 (Mix D45-T5) composites at 28 days of hydration. This technique gives vital information about the type and concentration of the formed phase. As indicated in Fig. 9-a, the TGA curve for OPC pastes illustrates three different stages (mass losses) at 50–300, 300–600 and 600–1000 °C, respectively and TG% for the 1st stage was 5.51% which indicates dehydrated/deteriorated amounts of C-S-Hs, C-A-S-Hs and C-A-Hs as the main binding silicates [83]. TG % of the 2nd loss was 5.65% due to decomposed amounts of free $Ca(OH)_2$ in addition to hydrogarnet phase (C-A-S-Hs) [84]. The last stage was about 3.27% due to the de-carbonation process. DSC technique confirmed three endothermic peaks at the mentioned three stages with energies (enthalpy) of 73.38, 29.58 and 3.23 J/g, respectively. Similar findings were reported in the investigation of Amin et al., 2015 [85]. On the other hand, the TGA curve for OPC paste containing 10 wt% DAK (D10) shows the same three stages. TG% for 1st, 2nd and last stage was 9.34%, 4.56% and 5.57%, respectively, Fig. 9-b. Moreover, the DSC curve show three endothermic peaks with energies of 87.72, 11.99 and 3.53 J/g, respectively. This date affirmed that the replacement of OPC by 10 wt% DAK increased the amount of binding silicates/hydrates from 5.51% to 9.34%. Simultaneously, a decrease in the amount of liberated lime from 5.51 to 4.56 due to

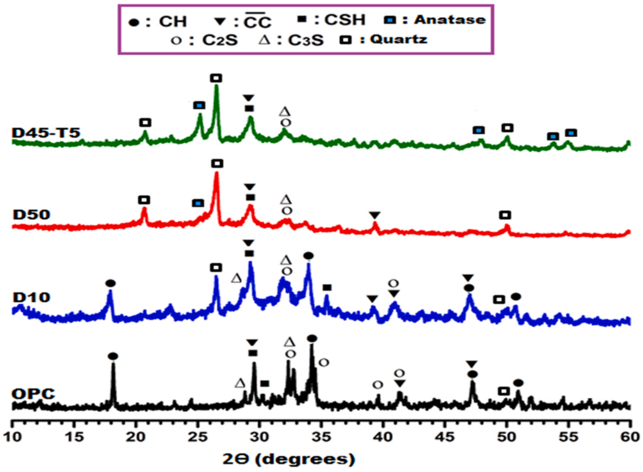

**Fig. 8.** XRD-patterns of OPC, OPC-10%DAK, OPC-50%DAK and OPC-45%DAK-5%$TiO_2$ composites at 28 days of hydration.

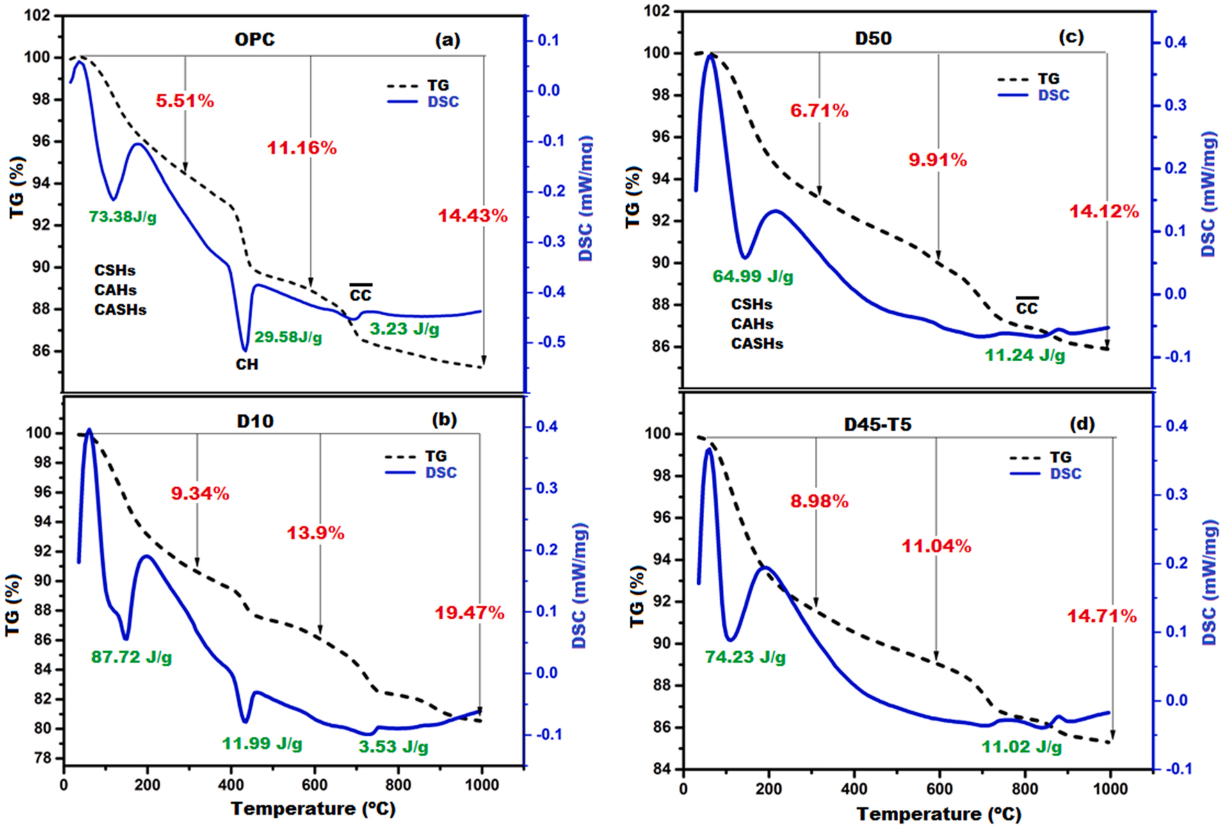

**Fig. 9.** TGA/DSC thermograms of OPC, OPC-10%DAK, OPC-50%DAK and OPC-45%DAK-5%$TiO_2$ composites at 28 days of hydration.

pozzolanic reaction was also noticed [86]. These outcomes are in line with the mechanical behavior of the D10 composite. Fig. 9-c clarifies the TGA thermogram for OPC paste containing 50 wt% DAK (Mix D50). The figure illustrates the same three losses. TG% was 6.71%, 3.20% and 4.21%, respectively. At the same time, the DSC curve indicates the disappearance of the Portland endothermic peak while the energies of the 1st and last endothermic peaks were 64.99 and 11.24 J/g, respectively. These results indicate that the high replacement of OPC by DAK negatively affected the amount of the formed binding silicate (ΔH decreased from 73.38 to 64.99 J/g) and the liberated lime (29.58 to zero J/g). Therefore, the compressive strength after 28-days of curing has been suppressed from 80 to 57.6 MPa. The same conclusions were reported by Palou et al., 2016 as the OPC was replaced by 35% SCMs (SF, GGBFS and MK) [87]. Fig. 9-d shows TGA/DSC thermograms for OPC containing 45%DAK + 5% $TiO_2$ as the anatase phase. The figure confirmed the vital role of the anatase phase on the progress of hydration reaction and generation of an extra amount of binding silicate [88]. After incorporating $TiO_2$, the 1st mass loss increased again from 6.71% to 8.98% and the corresponding energy also increased from 64.99 to 74.23 J/g. Hence, the compressive strength of the D45-T5 composite reached 88 MPa. Similar manner was observed in the study of Ma et al., 2016; the compressive strength of OPC+ 20% fly ash composite was enhanced in presence of 3%$TiO_2$ NPs which catalyzed the pozzolanic reaction and helped in the formation of C-S-Hs type of longer chains and higher Al:Si ratio [89].

### 3.4. *Textural characteristics*

This part aims to explain the micro-porosity after 28-days of hydration for some selected hardened composites (OPC, OPC-50%DAK and OPC-45%DAK-5%$TiO_2$) via the $N_2$-adsorption/desorption technique. The porous structure's identification may help explain the fabricated composites' mechanical properties and gamma-ray attenuation power. Textural parameters such as BET surface area ($cm^2/g$), BJH-average pore diameter (nm) and BJH-maximum pore diameter (dpmax, nm) were determined. These parameters strongly reflect the porous structure of the prepared composites. Six isotherms were classified according to IUPAC and three types of pores (micro, meso and macro). The structure with macro-pores possesses low surface area and high dpmax, while micro-pores containing structure possess large surface area and low dpmax. Meso-pores is considered intermediate type ($4 < \text{dpmax} < 100$ nm) [90]. Fig. 10 (a1-a3) displays adsorption-desorption isotherms for the selected composites. The isotherm type for OPC, OPC-50%DAK and OPC-45%DAK-5%$TiO_2$ is III/II, III and II, respectively. Mixed type (III/II) for OPC with H3-hysteresis loop while the composite containing 5% $TiO_2$ displays type II with H3-hysteresis loop. The appearance of the hysteresis loop is due to capillary condensation within the mesopores. OPC-50%DAK composite shows type III without hysteresis. Fig. 10 (b1, b3) illustrates pore size distribution curves for the selected composites according to the BJH model. It was found that dpmax values for OPC, OPC-50%DAK and OPC-45%DAK-5%$TiO_2$

were 59.47, 210 and 13.07 nm, respectively. Moreover, Table 3 clarifies the BET surface area for these composites and the values were 5960, 5030 and 14,141 $cm^2/g$, respectively. These results indicate that replacing OPC with 50 wt% DAK negatively affected the histological characteristics of generated composite (from meso to macro), while the inclusion of the 5 wt% $TiO_2$ contributed strongly to porous structure rearrangement from macro to macro meso. The anatase phase acted as a nano-filler which precipitated on the walls of the macro- pores in a regular manner and, at the same time, worked as nucleation sites/catalysts to generate additional hydration products (C-S-Hs, C-A-S-Hs, C-A-Hs) that also helped in narrowing the pores [91–93]. This data is very compatible with the mechanical trend of selected composites. D45-T5 has the highest compressive strength (88 MPa), highest surface area (14,141 $cm^2/g$) and lowest

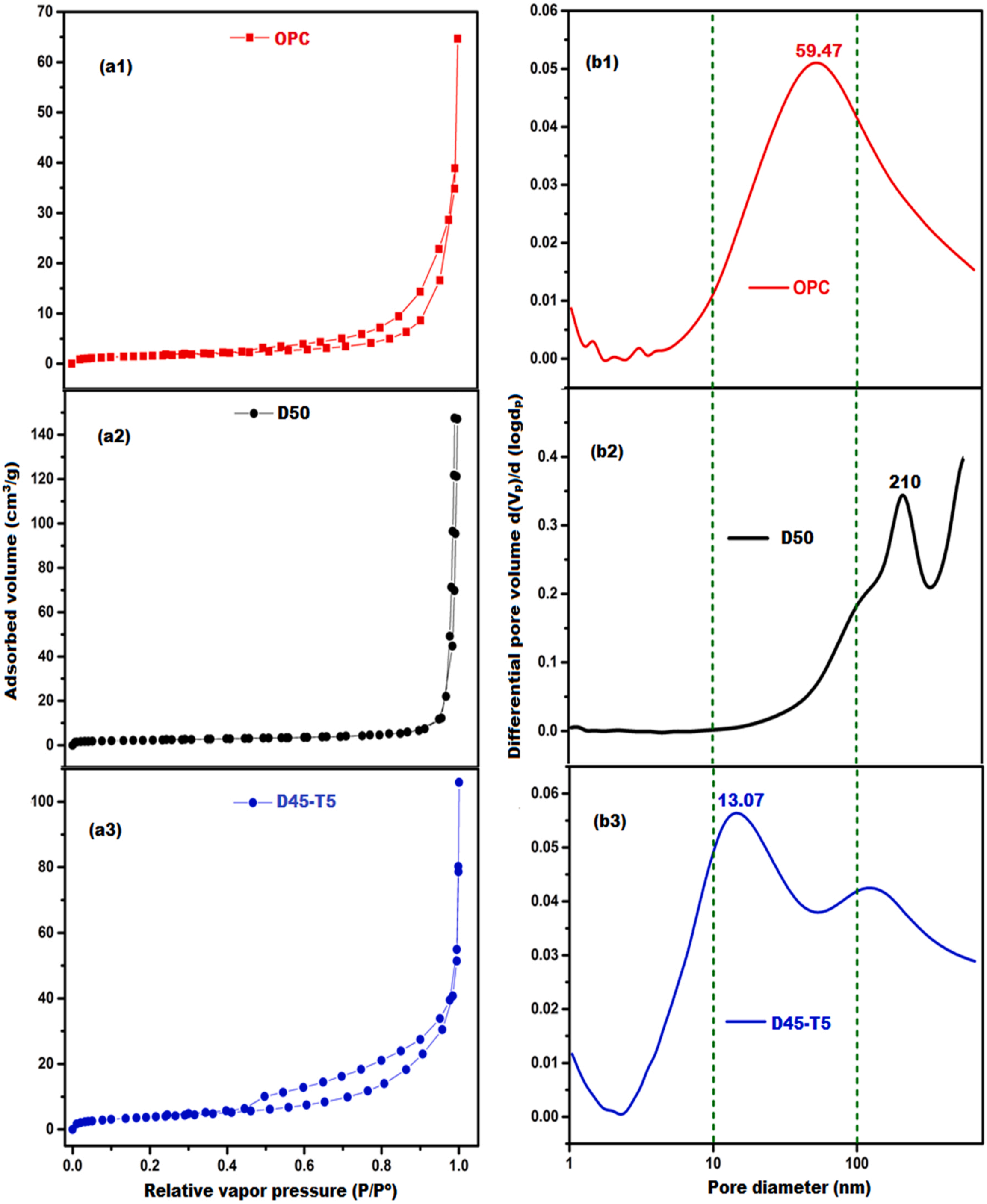

**Fig. 10.** BET isotherm/BJH model for: (a1, b1) OPC, (a2, b2) OPC-50%DAK, (a3, b3) OPC-45%DAK-5%$TiO_2$ composites at 28 days of hydration.

dpmax (13.07 nm). Other study confirmed that, by means of BET technique, the inclusion of 2.5% $TiO_2$ NPs could modify the porous structure of cement-mortar by changing the harmful large pores to the nano-sized pores, causing a lower permeability and higher durability, Shafaei et al., 2020 [94].

### 3.5. Morphology

Fig. 11 (a1, a2) displays SEM/EDX images for hydrated OPC pastes at 28-days hydration. The mesoporous structure was observed in the presence of precipitated needle crystals of C-S-Hs. Also, hexagonal shapes of Portlandite were mingled with the generated silicates [95]. The generated phases (CSHs, CH) are attributed to hydration of unreacted di/tri-calcium silicates (β-$C_2S$ and $C_3S$). The shape of CSHs (needles, fibers, rods, sheets, stacked plates) mainly depends on curing conditions (time, temperature, pressure, curing medium) as well as starting materials [96]. Almost, needle crystals appears in the first month as in case of OPC hydration and this observation is in line with the investigation of Hashem et al., 2021 [77]. The replacement of OPC by 10% DAK (Mix D10) led to a notable change in the morphology of CSHs (stacked plates and rods), Fig. 11 (b1, b2). Phase transformation is one of the most important reasons behind the development of mechanical efficacy of OPC-10% DAK composite; the same observation was studied by Zhang et al., 2018 [97]. Unreacted granules were observed after high substitution of OPC by DAK up to 50% (Mix D50) in the presence of little amounts of CSHs rods and calcite phase, Fig. 11 (c1, c2). The unreacted binders may be attributed to the existence of remained/inert kaolinite as a main phase inside DAK waste as well as unreacted silicates of OPC; the appearance of these phases caused a slight decay in the mechanical characteristics of D50 composite comparing with other composites; this outcome is matched with the work of Dixit et al., 2021 [98]. The incorporation of $TiO_2$ nanoparticles had an effective role in generating extra interlocked CSHs needles, which precipitated within the open porous structure to convert it into narrow mesoporous structure, so a dramatic development in the strength value of D45-T5 composite, Fig. 11 (d1, d2). The same behavior was reported by Yang et al., 2015 [99]. As displayed in EDX tables, Ca/Si ratios for OPC, D50 and D45-T5 were 13.29, 0.74 and 1.66, respectively. This means that composite D50 generated the lowest amount of CSHs. Moreover Al/Si ratios were 1.04, 0.17 and 0.17, respectively. These ratios confirm that composites D50 and D45-T5 have the lowest percentages of C-A-Hs. This is logical as these composites do not originally contain aluminum oxide [17,100].

### 3.6. Radiation shielding

Radiation shielding power against γ- rays for any shielding material is dependent on the crystallographic structure of included phases, microstructure (pore type, surface area), mechanical characteristic, source of gamma rays and operating temperature [28]. The value of the linear attenuation coefficient ($\mu$, $cm^{-1}$) strongly expresses the ability to attenuate gamma rays. The capability to mitigate gamma rays increases with increasing $\mu$ value. Only three composites were selected to perform this test: OPC, OPC-50%DAK and OPC-45DAK-5%$TiO_2$. According to Beer-Lambert law, Fig. 12 (a, b) shows the relation between transmitted intensity and thickness of the prepared paste. Whatever the source of gamma rays (Co-60 of high intensity and Cs-137 of low intensity), reverse relations with high fitting ($R^2 = 0.990$–$0.996$) were obtained for all selected composites. The standard deviation of the measurement did not exceed 0.007. These values confirm the strong validation of the beer-lambert law on the prepared composites. Fig. 13 shows the linear attenuation coefficient values at low (661.6Kev) and high intensity (1332.5 Kev) for OPC, D50 and D45-T5 composites. The figure indicates the high replacement of OPC by 50%DAK (D50) affected negatively on the attenuation ability; as the linear attenuation coefficient values were suppressed from $0.127 \pm 0.003$ $cm^{-1}$ to $0.105 \pm 0.003$ $cm^{-1}$ at 661.6 Kev and from $0.118 \pm 0.003$ $cm^{-1}$ to $0.086 \pm 0.002$ $cm^{-1}$ at 1332.5 Kev, Meanwhile, the inclusion of 5% Anatase nanoparticles (D45-T5 composite) has great impact on the development of shielding power; as $\mu$ values were enhanced from $0.127 \pm 0.003$ $cm^{-1}$ to $0.199 \pm 0.007$ $cm^{-1}$ at 661.6 Kev and from $0.118 \pm 0.003$ $cm^{-1}$ to $0.144 \pm 0.005$ $cm^{-1}$ at 1332.5 Kev. These results can be explained in Fig. 14, in which a strong correlation between attenuation power, mechanical and textural characteristics. As shown in the figure, the attenuation % (at low intensity) decreased to 82.7% when OPC was replaced by 50% DAK, as the high replacement caused a sudden change in histological and mechanical characteristics. Pores enlargement from 57.5 nm to 210 nm and decay in the strength value from 80 to 57.6 MPa, so the penetration power of gamma rays has been elevated. On the other hand, adding 5%TiO2 NPs (composite D45-T5) caused a strong boosting in the attenuation % to 156.7 compared with OPC. Anatase phase acted as a nano-filler which precipitated on the walls of the macro- pores in a regular manner and at the same time worked as a catalyst to generate additional hydration products (CSHs, CASHs, CAHs) that also helped in narrowing the pores from 210 nm to 13.07, so the shielding power in case of D45-T5 has been elevated. Moreover, the crystallographic structure of tetragonal anatase is considered one of the most important factors that made $TiO_2$ NPs act as dosimetric material of super absorbent capacity against penetrable gamma rays [1,44,45].

**Table 3**
Textural parameters for some selected pastes at 28 days of hydration.

| Selected composite | BET surface area ($cm^2/g$) | BJH average pore diameter (nm) | Max pore diameter $dp_{max}$ (nm) | Pore type |
|---|---|---|---|---|
| OPC | 5690 | 25.47 | 59.47 | Meso |
| D50 | 5030 | 128.56 | 210 | Macro |
| D45-T5 | 14,141 | 15.83 | 13.07 | Meso |

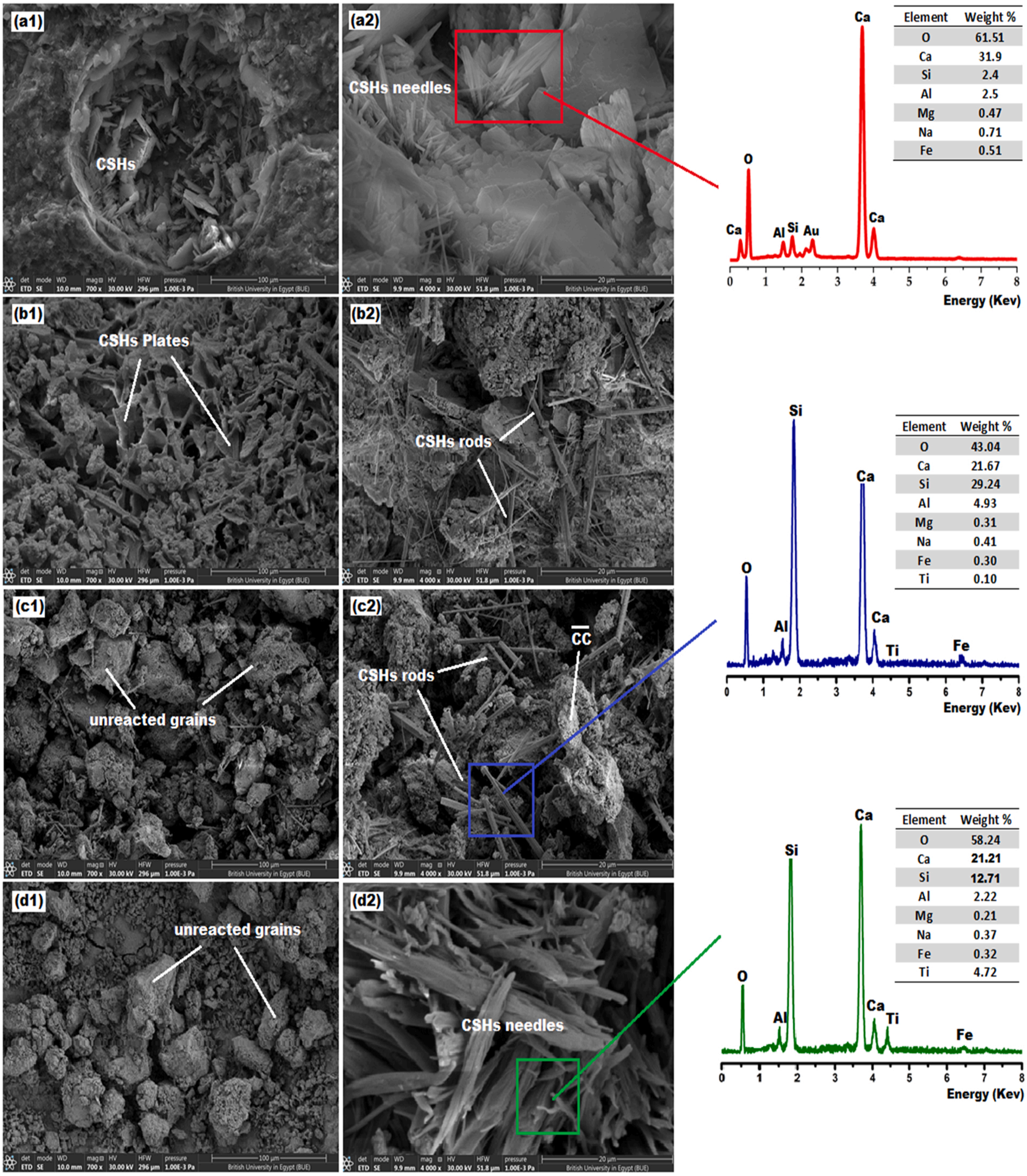

| Element | Weight % |
|---|---|
| O | 61.51 |
| Ca | 31.9 |
| Si | 2.4 |
| Al | 2.5 |
| Mg | 0.47 |
| Na | 0.71 |
| Fe | 0.51 |

| Element | Weight % |
|---|---|
| O | 43.04 |
| Ca | 21.67 |
| Si | 29.24 |
| Al | 4.93 |
| Mg | 0.31 |
| Na | 0.41 |
| Fe | 0.30 |
| Ti | 0.10 |

| Element | Weight % |
|---|---|
| O | 58.24 |
| Ca | 21.21 |
| Si | 12.71 |
| Al | 2.22 |
| Mg | 0.21 |
| Na | 0.37 |
| Fe | 0.32 |
| Ti | 4.72 |

**Fig. 11.** SEM/EDX images of (a1, a2) OPC, (b1, b2) OPC-10%DAK, (c1, c2) OPC-50%DAK and (d1, d2) OPC-45%DAK-5%$TiO_2$ composites at 28 days of hydration.

## 4. Conclusion

The main objective of this study is to use commercial titania to improve the mechanical properties of blended cement containing large percentages of dealuminated kaolin (DAK) to produce sustainable and eco-friendly building materials; where all previous studies have proven that using large percentages of DAK (beyond 10 wt%) as a cement replacement has a negative effect on the properties of cement. The impact of using different DAK wt% and commercial $TiO_2$ on the workability, mechanical properties, phase composition, microstructure and texture characteristics of the fabricated blended cement pastes was measured. Also, to achieve the maximum

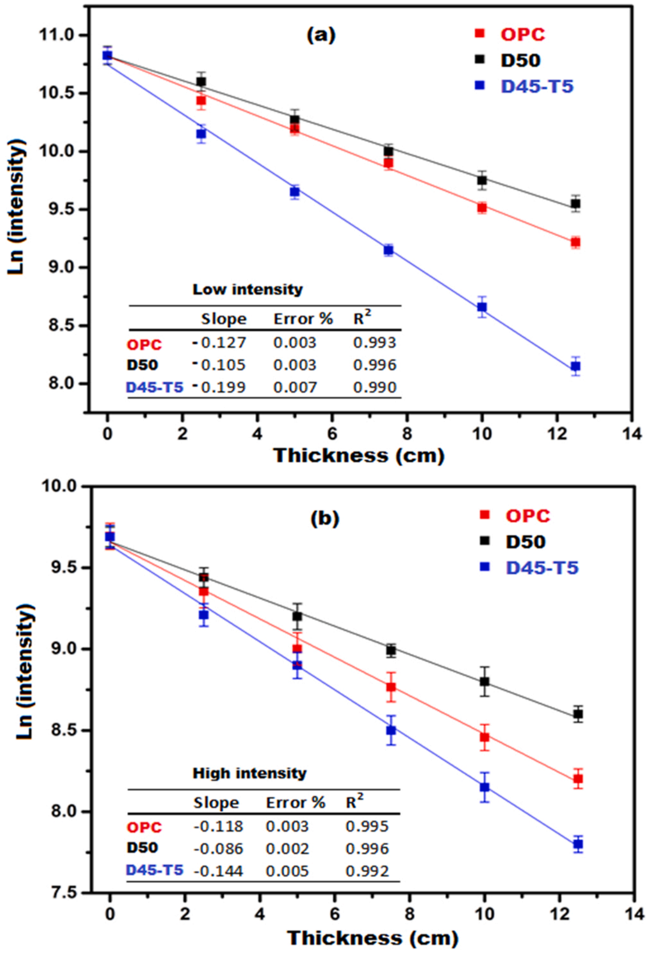

Low intensity

| | Slope | Error % | $R^2$ |
|---|---|---|---|
| OPC | -0.127 | 0.003 | 0.993 |
| D50 | -0.105 | 0.003 | 0.996 |
| D45-T5 | -0.199 | 0.007 | 0.990 |

High intensity

| | Slope | Error % | $R^2$ |
|---|---|---|---|
| OPC | -0.118 | 0.003 | 0.995 |
| D50 | -0.086 | 0.002 | 0.996 |
| D45-T5 | -0.144 | 0.005 | 0.992 |

**Fig. 12.** Relation between transmitted intensity and thickness of some selected composites (a) Cs-137 isotope (b) Co-60 isotope.

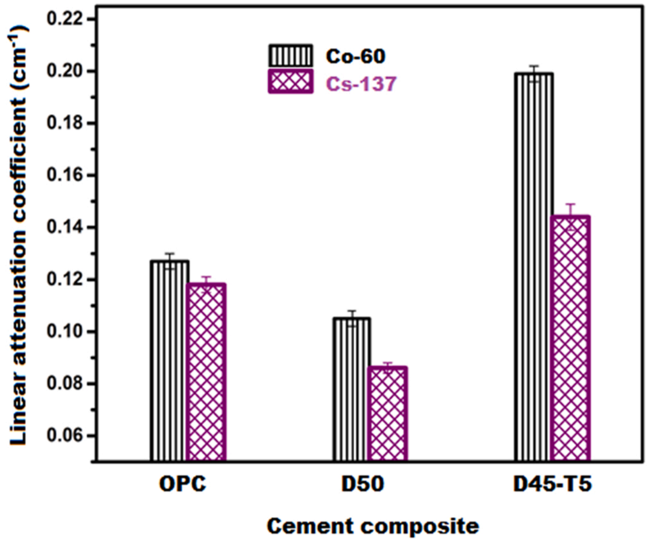

**Fig. 13.** Linear attenuation coefficient values for some selected composites at different gamma source.

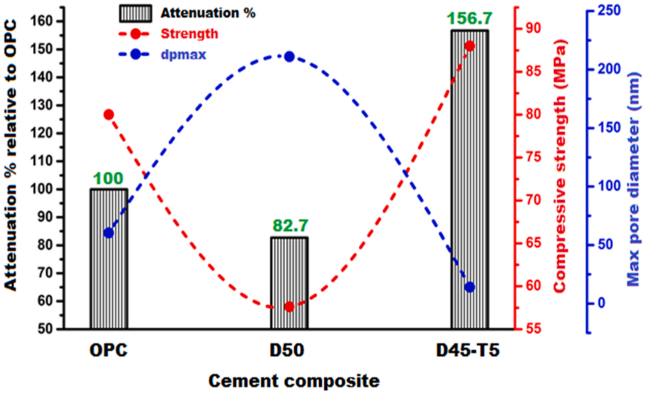

**Fig. 14.** Correlation between attenuation %, compressive strength and max pore diameter for some selected composites at 661.6 Kev.

possible benefit from commercial titania, its effect on the linear attention coefficient was assessed to investigate the material's applicability in protection against harmful gamma-ray radiation. The results obtained showed the following:

- A high water/binder ratio and superplasticizer percentage are required for fresh DAK-blended cement pastes to achieve the same workability as control paste (100 wt% OPC) due to the high surface area and small particle size of DAK compared to cement.
- Replacement of OPC with 10 wt% DAK increased the compressive strength by 16.4% due to pozzolanic activity, inert filling effect and good dispersion of DAK in the cement matrix. In contrast, increasing replacement up to 30 and 50 wt% decreased the compressive strength by 23.7% and 26.7% at 28 days, respectively, resulting from the high dilution of cement.
- Only 5 wt% $TiO_2$ is enough to partially replace DAK in the D50 specimen (as in 50%OPC-45%DAK-5%$TiO_2$ specimen) to attain a higher compressive strength than the control paste (100 wt% OPC) as $TiO_2$ acts as an active site for the formation of more hydration products and its small particle size caused pore structure redistribution that is resulting in compacting composition.
- XRD-pattern clarified that $TiO_2$ does not have a cementitious characteristic and its effect in enhancing the mechanical properties is referred to its high surface area.
- The $N_2$ adsorption-desorption isotherms showed that the isotherm type for control, D50 and D45-T5, is macro/meso, macro and meso, respectively, which clarifies the role of $TiO^2$ in pore size redistribution and then enhances the compressive strength.
- $TiO_2$ particles successfully generated extra interlocked C-S-Hs needles, which strengthened the microstructure of the D45-T5 composite. Also, SEM showed a narrowing of the pore size in the case of D45-T5 than D50, which confirms changes in the texture characteristics from macro to meso pores obtained by $N_2$ adsorption-desorption isotherms.
- Replacement of OPC with 50 wt% DAK has a detrimental effect on the radiation shielding efficiency, as it decreases the linear attention coefficient by 17.3% and 27.1% than the control specimen (100% OPC) using gamma-ray intensities of 661.6 and 1332.5 Kev, respectively. While the incorporation of $TiO_2$ led to increases in the linear attention coefficient by 56.7% and 22% at the same intensities. This phenomena were discussed by making a correlation between texture characteristics, mechanical properties and attenuation coefficient. Small pores size increases the compressive strength and formed compact structure and then translated into high linear attenuation coefficient.

## Declaration of Competing Interest

The authors declare that they have no known competing financial interests or personal relationships that could have appeared to influence the work reported in this paper.

## Data Availability

I want to share may article with researcher.

## Acknowledgments

The authors extend their appreciation to Researchers Supporting Project number (RSP-2021/271), King Saud University, Riyadh, Saudi Arabia.

## References

[1] M. Ramadan, W. Ramadan, F. Shwita, N. El-Faramawy, Valorization of hazardous glass wastes via geopolymer production utilized in gamma ray shielding applications: a comparative study with Portland cement, 2022/08/01/, Radiat. Phys. Chem. vol. 197 (2022), 110174, 2022/08/01/.

[2] G. Tyagi, A. Singhal, S. Routroy, D. Bhunia, M. Lahoti, Radiation Shielding Concrete with alternate constituents: An approach to address multiple hazards, J. Hazard. Mater. vol. 404 (2021), 124201.

[3] Ł. Skarżyński, Mechanical and radiation shielding properties of concrete reinforced with boron-basalt fibers using Digital Image Correlation and X-ray micro-computed tomography, Constr. Build. Mater. vol. 255 (2020), 119252.

[4] M. Papachristoforou, I. Papayianni, Radiation shielding and mechanical properties of steel fiber reinforced concrete (SFRC) produced with EAF slag aggregates, Radiat. Phys. Chem. vol. 149 (2018) 26–32.

[5] A.A. El Gindy, E.A. Gomaa, H.I. Abdelkader, A. Mohsen, A.O. Habib, The effect of a sulfonated naphthalene-based polymer on redox reaction data, potassium ferrocyanide complexation, and the compressive strength of Portland cement paste, J. Mol. Liq. vol. 356 (2022), 119000.

[6] O.A. Mayhoub, A. Mohsen, Y.R. Alharbi, A.A. Abadel, A.O. Habib, M. Kohail, Effect of curing regimes on chloride binding capacity of geopolymer, 2021/05/19/, Ain Shams Eng. J. (2021), 2021/05/19/.

[7] A. Mohsen, M.S. El-Feky, A.M. El-Tair, M. Kohail, Effect of delayed microwaving on the strength progress of Green alkali activated cement composites, J. Build. Eng. vol. 43 (2021), 103135.

[8] M. Refaat, A. Mohsen, E.-S.A.R. Nasr, M. Kohail, Minimizing energy consumption to produce safe one-part alkali-activated materials, J. Clean. Prod. vol. 323 (2021), 129137.

[9] M.S. El-Feky, A. Mohsen, A. Maher El-Tair, M. Kohail, Microstructural investigation for micro - nano-silica engineered magnesium oxychloride cement, Constr. Build. Mater. vol. 342 (2022), 127976.

[10] ASTMC595/08a Standard Specification for Blended Hydraulic Cements Annu. Book ASTM Stand. 2010.

[11] A.O. Habib, I. Aiad, F.I. El-Hosiny, A. Mohsen, Studying the impact of admixtures chemical structure on the rheological properties of silica-fume blended cement pastes using various rheological models, Ain Shams Eng. J. vol. 12 (2) (2021) 1583–1594.

[12] B. Kondraivendhan, B. Bhattacharjee, Flow behavior and strength for fly ash blended cement paste and mortar, Int. J. Sustain. Built Environ. vol. 4 (2) (2015) 270–277.

[13] C.B. Cheah, J.J. Liew, K. Khaw Le Ping, R. Siddique, W. Tangchirapat, Properties of ternary blended cement containing ground granulated blast furnace slag and ground coal bottom ash, Constr. Build. Mater. vol. 315 (2022), 125249.

[14] S.A. Zareei, F. Ameri, F. Dorostkar, M. Ahmadi, Rice husk ash as a partial replacement of cement in high strength concrete containing micro silica: Evaluating durability and mechanical properties, Case Stud. Constr. Mater. vol. 7 (2017) 73–81.

[15] A. Mohsen, I. Aiad, F.I. El-Hossiny, A.O. Habib, Evaluating the mechanical properties of admixed blended cement pastes and estimating its kinetics of hydration by different techniques, Egypt. J. Pet. vol. 29 (2) (2020) 171–186.

[16] A. Eldeeb, V. Brichkin, Egypt. Alum. Contain. ores Prospects their Use Prod. Alum. vol., 9, 2020, pp. 722–731.

[17] S.A. Abo-El-Enein, M. Heikal, M.S. Amin, H.H. Negm, Reactivity of dealuminated kaolin and burnt kaolin using cement kiln dust or hydrated lime as activators, Constr. Build. Mater. vol. 47 (2013) 1451–1460.

[18] G. Abdelaziz, A. Abdelalim, H. Ghorab, M. Elsayed, Characterization of OPC Matrix Containing Dealuminated Kaolin, 01/01, J. Cem. Wapno Beton vol. 1 (2011), 01/01.

[19] A. Ababneh, F. Matalkah, B. Matalkeh, Effects of kaolin characteristics on the mechanical properties of alkali-activated binders, Constr. Build. Mater. vol. 318 (2022), 126020.

[20] R. Fernandez, F. Martirena, K.L. Scrivener, The origin of the pozzolanic activity of calcined clay minerals: a comparison between kaolinite, illite and montmorillonite, Cem. Concr. Res. vol. 41 (1) (2011) 113–122.

[21] L. Chen, Z. Wang, Y. Wang, J. Feng, Preparation and properties of alkali activated metakaolin-based geopolymer, Materials vol. 9 (9) (2016).

[22] M. Abdelmawla, A. Abdelaal, M. Beheary, N. Abdullah, T.M.A. Razek, Solidification of alum industry waste for producing geopolymer mortar, Egypt. J. Chem. 04/01 (2020).

[23] S.A. Jagtap, M.N. Shirsath, S.L. Karpe, Effect of metakaolin on the properties of concrete, Int. Res. J. Eng. Technol. vol. 4 (7) (2017) 643–645.

[24] R. Muduli, B.B. Mukharjee, Effect of incorporation of metakaolin and recycled coarse aggregate on properties of concrete, 10/01, J. Clean. Prod. vol. 209 (2018), 10/01.

[25] B. Amrane, K. Souici, B. Hami, S. Kennouche, B. Safi, N. Mesrati, Eff. metakaolin Partial. Cem. Replace. Compress. Strength Stand. Mortars vol. 12, 2021, pp. 268–280.

[26] S. Zhang, Y. Zhou, J. Sun, F. Han, Effect of ultrafine metakaolin on the properties of mortar and concrete, Crystals vol. 11 (2021) 665.

[27] Z. Zidi, M. Ltifi, I. Zafar, Synthesis and attributes of nano-SiO2 local metakaolin based-geopolymer, J. Build. Eng. vol. 33 (2021), 101586.

[28] A. Mohsen, H.A. Abdel-Gawwad, M. Ramadan, Performance, radiation shielding, and anti-fungal activity of alkali-activated slag individually modified with zinc oxide and zinc ferrite nano-particles, Constr. Build. Mater. vol. 257 (2020), 119584.

[29] N. Muisa, I. Nhapi, W. Ruziwa, M.M. Manyuchi, Utilization of alum sludge as adsorbent for phosphorus removal in municipal wastewater: a review, J. Water Process Eng. vol. 35 (2020), 101187.

[30] A.M.K. Abdelalim, H.Y. Ghorab, G. Abdelaziz, M.S. Elsayed, Dealuminated kaolin as cement replacement material, J. Cem. Wapno Beton vol. 15 (2008) 132–140.

[31] N.Y. Mostafa, S.A.S. El-Hemaly, E.I. Al-Wakeel, S.A. El-Korashy, P.W. Brown, Characterization and evaluation of the pozzolanic activity of Egyptian industrial by-products: I: Silica fume and dealuminated kaolin, Cem. Concr. Res. vol. 31 (3) (2001) 467–474.

[32] H. Moselhy, Effect of dealuminated kaolin waste on slump and compressive strength for ordinary Portland cement concrete, Int. J. Chem. Eng. vol. 10 (2) (2018).

[33] Z. Ren, et al., Optimizing the content of nano-SiO2, nano-TiO2 and nano-CaCO3 in Portland cement paste by response surface methodology, J. Build. Eng. vol. 35 (2021), 102073.

[34] Z. Wang, Q. Yu, F. Gauvin, P. Feng, R. Qianping, H.J.H. Brouwers, Nanodispersed TiO2 hydrosol modified Portland cement paste: The underlying role of hydration on self-cleaning mechanisms, Cem. Concr. Res. vol. 136 (2020), 106156.

[35] K. Wang, X. Zha, Effect of nano-TiO2 content on the flexural strength and compressive strength of dry-Mixing CDG-Slag based geopolymer paste, in: IOP Conference Series: Materials Science and Engineering, vol. 720, IOP Publishing, 2020, 012002.

[36] Z. Li, et al., Effect of nano-titanium dioxide on mechanical and electrical properties and microstructure of reactive powder concrete, Mater. Res. Express vol. 4 (9) (2017), 095008.

[37] M. Daniyal, S. Akhtar, A. Azam, Effect of nano-TiO2 on the properties of cementitious composites under different exposure environments, J. Mater. Res. Technol. vol. 8 (6) (2019) 6158–6172.

[38] A. Joshaghani, M. Balapour, M. Mashhadian, T. Ozbakkaloglu, Effects of nano-TiO2, nano-Al2O3, and nano-Fe2O3 on rheology, mechanical and durability properties of self-consolidating concrete (SCC): an experimental study, Constr. Build. Mater. vol. 245 (2020), 118444.

[39] L. Qiang, Preparation of nano-TiO2 by waste clay bricks and photocatalytic effect on concrete, Emerg. Mater. Res. vol. 9 (3) (2020) 839–850.

[40] Z. Guo, C. Huang, Y. Chen, Experimental study on photocatalytic degradation efficiency of mixed crystal nano-TiO2 concrete, Nanotechnol. Rev. vol. 9 (2020) 219–229.

[41] G. Singh, et al., Impact of TiO2 on radiation shielding competencies and structural, physical and optical properties of CeO2-PbO-B2O3 glasses, J. Alloy. Compd. vol. 885 (2021), 160939.

[42] A. Askin, M.H.M. Zaid, O. Stephen, M. Khandaker, D. Chushkova, D. Bradley, Radiation shielding and mechanical properties of Bi2O3-Na2O-TiO2-ZnO-TeO2 glass system, 05/01, Radiat. Phys. Chem. vol. 186 (2021), 109556, 05/01.

[43] K.H. Mahmoud, K.A. Elsayed, E.A.A. Wahab, F.M. Abdel-Rahim, K.S. Shaaban, Structural and radiation shielding simulation of B2O3–SiO2–LiF–ZnO–TiO2 glasses, J. Mater. Sci.: Mater. Electron. vol. 32 (12) (2021) 16182–16193.

[44] I.M. Nikbin, R. Mohebbi, S. Dezhampanah, S. Mehdipour, R. Mohammadi, T. Nejat, Gamma ray shielding properties of heavy-weight concrete containing Nano-TiO2, Radiat. Phys. Chem. vol. 162 (2019) 157–167.

[45] S. Dezhampanah, M. Iman, S. Mehdipour, R. Mohebbi, H. Moghadam, Fiber- reinforced concrete containing nano - TiO2 as a new gamma-ray radiation shielding materials, J. Build. Eng. vol. 44 (2021), 102542.

[46] M. Iman, et al., Effect of high temperature on mechanical and gamma ray shielding properties of concrete containing nano-TiO2, Radiat. Phys. Chem. vol. 174 (2020), 108967.

[47] J. Park, S. Heongwon, M. Woo, K. Jeong, S. Seok, Assessment of neutron shielding performance of nano-TiO 2 -incorporated cement paste by Monte Carlo simulation, 05/05, Prog. Nucl. Energy vol. 117 (2019), 05/05.

[48] EN450-1, Fly ash for concrete. Part 1: Definition, and specifications and criteria, European Committee for Standardisation CEM, *Brussels*, 2012.

[49] M. Wojtkowska, Ł. Szarek, Properties of fl y ash from thermal treatment of municipal sewage sludge in terms of EN 450-1, 02/24, Arch. Environ. Prot. vol. 44 (2018), 02/24.

[50] L.A. Silva, B.O. Nahime, E.C. Lima, J. Akasaki, I.C. Reis, XRD investigation of cement pastes incorporating concrete floor polishing waste, Cerâmica vol. 66 (2020) 373–378.

[51] H.F. Taylor, Cement Chemistry, Thomas Telford London, 1997.

[52] W. Nigussie, F. Zewge, B.S. Chandravanshi, Removal of excess fluoride from water using waste residue from alum manufacturing process, J. Hazard. Mater. vol. 147 (3) (2007) 954–963.

[53] K. Yan, Y. Guo, L. Fang, L. Cui, F. Cheng, T. Li, Decomposition and phase transformation mechanism of kaolinite calcined with sodium carbonate, Appl. Clay Sci. vol. 147 (2017) 90–96.

[54] P. Sikora, K. Cendrowski, A. Markowska-Szczupak, E. Horszczaruk, E. Mijowska, The effects of silica/titania nanocomposite on the mechanical and bactericidal properties of cement mortars, Constr. Build. Mater. vol. 150 (2017) 738–746.

[55] K. Loh, C. Gaylarde, M. Shirakawa, Photocatalytic activity of ZnO and TiO2 'nanoparticles' for use in cement mixes, Constr. Build. Mater. vol. 167 (2018) 853–859.

[56] H. Elshimy, T. Abdallah, A.A. Shama, Optimization of spin coated TiO2 layer for hole-free perovskite solar cell, IOP Conf. Ser.: Mater. Sci. Eng. vol. 762 (1) (2020), 012003.

[57] H. Elshimy, T. Abdallah, The effect of mechanically milled lead iodide powder on perovskite film morphology, Appl. Phys. A vol. 128 (1) (2021) 33.

[58] P. Periyat, D.E. McCormack, S.J. Hinder, S.C. Pillai, One-pot synthesis of anionic (nitrogen) and cationic (sulfur) codoped high-temperature stable, visible light active, anatase photocatalysts, J. Phys. Chem. C vol. 113 (8) (2009) 3246–3253.

[59] ASTMC1161-18 Standard test method for slump flow of self-consolidating concrete Annu. Book ASTM Stand. 2009.

[60] ASTMC109M-20b, Standard test method for compressive strength of hydraulic cement mortars (using 2-in. or [50-mm] cube specimens, Annu. Book ASTM Stand. (2020).

[61] A.O. Habib, I. Aiad, T.A. Youssef, A.M. Abd El-Aziz, Effect of some chemical admixtures on the physico-chemical and rheological properties of oil well cement pastes, Constr. Build. Mater. vol. 120 (2016) 80–88.

[62] B. Felekoğlu, H. Sarıkahya, Effect of chemical structure of polycarboxylate-based superplasticizers on workability retention of self-compacting concrete, Constr. Build. Mater. vol. 22 (9) (2008) 1972–1980.

[63] Y. Ouldkhaoua, B. Benabed, R. Abousnina, E.-H. Kadri, Experimental study on the reuse of cathode ray tubes funnel glass as fine aggregate for developing an ecological self-compacting mortar incorporating metakaolin, J. Build. Eng. vol. 27 (2020), 100951.

[64] A.O. Habib, I. Aiad, F.I. El-Hosiny, A.M. Abd El-Aziz, Development of the fire resistance and mechanical characteristics of silica fume-blended cement pastes using some chemical admixtures, Constr. Build. Mater. vol. 181 (2018) 163–174.

[65] N. Mostafa, M. Qhatani, S.A.S. El-Hemaly, S. El-Korashy, P.W. Brown, High replacements of reactive pozzolan in blended cements: microstructure and mechanical properties, Cem. Concr. Compos. vol. 32 (2010) 386–391.

[66] H. Bendary, M. Abadir, H. Moselhy, H.J.I.J.C.E.R. Ghazal, Effect of alum waste addition on the fluidity, initial and finial setting and compressive strength of ordinary Portland cement mortar, Int. J. Chem. Eng. Res. vol. 9 (1) (2017) 89–98.

[67] J.D. Macedo, C.J.A. Mota, S.M.C. de Menezes, V. Camorim, NMR and acidity studies of dealuminated metakaolin and their correlation with cumene cracking, Appl. Clay Sci. vol. 8 (5) (1994) 321–330.

[68] N. Mostafa, S. El-Hemaly, E. Al-Wakeel, S. El-Korashy, P. Brown, Activity of silica fume and dealuminated kaolin at different temperatures, Cem. Concr. Res. vol. 31 (2001) 905–911.

[69] A. Bentur, Effect of Gypsum on the Hydration and Strength of C3S Pastes, J. Am. Ceram. Soc. vol. 59 (1976) 210–213.

[70] S.A.S. E$\ell$-Hemaly, K. Mohan, H.F.W. Taylor, Autoclaved lime — quartz materials II. Thermogravimetry and trimethylsilylation, Cem. Concr. Res. vol. 8 (6) (1978) 671–676.

[71] F. Majstorovic, V. Sebera, M. Mrak, S. Dolenec, M. Wolf, L. Marrot, Impact of metakaolin on mechanical performance of flax textile-reinforced cement-based composites, Cem. Concr. Compos. vol. 126 (2021), 104367.

[72] H. Li, M.-h Zhang, J.-p Ou, Abrasion resistance of concrete containing nano-particles for pavement, Wear vol. 260 (11) (2006) 1262–1266.

[73] J. Sun, et al., Studies on the size effects of nano-TiO2 on Portland cement hydration with different water to solid ratios, Constr. Build. Mater. vol. 259 (2020), 120390.

[74] R. Zhang, X. Cheng, P. Hou, Z. Ye, Influences of nano-TiO2 on the properties of cement-based materials: Hydration and drying shrinkage, Constr. Build. Mater. vol. 81 (2015) 35–41.

[75] S.M.A. El-Gamal, S.A. Abo-El-Enein, F.I. El-Hosiny, M.S. Amin, M. Ramadan, Thermal resistance, microstructure and mechanical properties of type I Portland cement pastes containing low-cost nanoparticles, J. Therm. Anal. Calorim. vol. 131 (2) (2018) 949–968.

[76] S.A. Abo-El-Enein, F.I. El-Hosiny, S.M.A. El-Gamal, M.S. Amin, M. Ramadan, Gamma radiation shielding, fire resistance and physicochemical characteristics of Portland cement pastes modified with synthesized $Fe_2O_3$ and ZnO nanoparticles, Constr. Build. Mater. vol. 173 (2018) 687–706.

[77] F. Hashem, E. Hekal, M. Abdelnaby, F. Selim, Mechanical properties and durability performance against fire, gamma ray and bio-fouling of hardened Portland cement pastes incorporating lead bearing wastes, 07/16, Mater. Chem. Phys. vol. 272 (2021), 07/16.

[78] M. Heikal, M. Zaki, S.M. Ibrahim, Characterization, hydration, durability of nano-Fe2O3-composite cements subjected to sulphates and chlorides media, Constr. Build. Mater. vol. 269 (2020), 121310.

[79] M. Ramadan, M. Amin, M. Abdellah, Superior physico-mechanical, fire resistivity, morphological characteristics and gamma radiation shielding of hardened OPC pastes incorporating $ZnFe_2O_4$ spinel nanoparticles, Constr. Build. Mater. vol. 234 (2020), 117807.

[80] S.M.A. Gamal, F.I. Elhosiny, M. Amin, D. Gamal, Ceramic waste as an efficient material for enhancing the fire resistance and mechanical properties of hardened Portland cement pastes, 11/15, Constr. Build. Mater. vol. 154 (2017), 11/15.

[81] C. Luan, et al., Effects of nano-SiO2, nano-CaCO3 and nano-TiO2 on properties and microstructure of the high content calcium silicate phase cement (HCSC), Constr. Build. Mater. vol. 314 (2022), 125377.

[82] B.Y. Lee, K. Kurtis, Influence of TiO2 nanoparticles on early C3S hydration, J. Am. Ceram. Soc. vol. 93 (2010) 3399–3405.

[83] M. Ramadan, S.M.A. El-Gamal, F.A. Selim, Mechanical properties, radiation mitigation and fire resistance of OPC-recycled glass powder composites containing nanoparticles, Constr. Build. Mater. vol. 251 (2020), 118703.

[84] A. Mohsen, M. Ramadan, M. Gharieb, A. Yahya, A. Soltan, M.M. Hazem, Rheological behaviour, mechanical performance, and anti-fungal activity of OPC-granite waste composite modified with zinc oxide dust, J. Clean. Prod. vol. 341 (2022), 130877.

[85] M. Amin, S.M.A. Gamal, F. Hashem, Fire resistance and mechanical properties of carbon nanotubes - clay bricks wastes (Homra) composites cement, Constr. Build. Mater. vol. 98 (2015) 237–248.

[86] S.M.A. El-Gamal, M.S. Amin, M. Ramadan, Hydration characteristics and compressive strength of hardened cement pastes containing nano-metakaolin, HBRC J. vol. 13 (1) (2017) 114–121.

[87] M.T. Palou, E. Kuzielová, R. Novotný, F. Šoukal, M. Žemlička, Blended cements consisting of Portland cement–slag–silica fume–metakaolin system, J. Therm. Anal. Calorim. vol. 125 (3) (2016) 1025–1034.

[88] F. Shwita, N. El-Faramawy, W. Ramadan, M. Ramadan, Investigation of the mechanical properties, morphology and the attenuation behavior of gamma rays for OPC pastes mingled with two different glass wastes, Constr. Build. Mater. vol. 313 (2021), 125475.

[89] B. Ma, H. Li, X. Li, J. Mei, Y. Lv, Influence of nano-TiO2 on physical and hydration characteristics of fly ash–cement systems, Constr. Build. Mater. vol. 122 (2016) 242–253.

[90] N. Lee, H. Khalid, H.K. Lee, Synthesis of mesoporous geopolymers containing zeolite phases by a hydrothermal treatment, Microporous Mesoporous Mater. vol. 229 (2016) 22–30.

[91] H. Mohamed, et al., Mechanical and microstructural properties of geopolymer mortars from meta-halloysite: effect of titanium dioxide TiO2 (anatase and rutile) content, SN Appl. Sci. vol. 2 (9) (2020) 1–14.

[92] C. Mendoza, A. Valle, M. Castellote, A. Bahamonde, M. Faraldos, TiO2 and TiO2 –SiO2 coated cement: comparison of mechanic and photocatalytic properties, Appl. Catal. B: Environ. vol. 178 (2014) 155–164.

[93] A. Maher, M. Elfeky, A. Mohsen, M. Kohail, Properties of nano engineered concrete subjected to accelerated corrosion, Nanotechnol. Constr. A Sci. Internet-J. vol. 13 (2021) 293–305.

[94] D. Shafaei, S. Yang, L. Berlouis, J. Minto, Multiscale pore structure analysis of nano titanium dioxide cement mortar composite, Mater. Today Commun. vol. 22 (2020), 100779.

[95] F. Selim, M. Amin, M. Ramadan, M. Hazem, Effect of elevated temperature and cooling regimes on the compressive strength, microstructure and radiation attenuation of fly ash–cement composites modified with miscellaneous nanoparticles, Constr. Build. Mater. vol. 258 (2020), 119648.

[96] M. Frías, S. Martínez-Ramírez, R. Villa, R. García-Giménez, M. Rojas, New scientific evidence of the effect of high temperatures and long curing times on MK-blended cement paste mineralogy, Cem. Concr. Res. vol. 152 (2022), 106657.

[97] Z. Zhang, G. Scherer, A. Bauer, Morphology of cementitious material during early hydration, Cem. Concr. Res. vol. 107 (2018) 85–100.

[98] A. Dixit, H. Du, S.D. Pang, Performance of mortar incorporating calcined marine clays with varying kaolinite content, J. Clean. Prod. vol. 282 (2021), 124513.

[99] L.Y. Yang, Z. Jia, Y.M. Zhang, Effects of nano-TiO2 on strength, shrinkage and microstructure of alkali activated slag pastes, 03/31, Cem. Concr. Compos. vol. 57 (2015), 03/31.

[100] M. Ramadan, M.S. Amin, S.A. Waly, A. Mohsen, Effect of high gamma radiation dosage and elevated temperature on the mechanical performance of sustainable alkali-activated composite as a cleaner product, Cem. Concr. Compos. vol. 121 (2021), 104087.